



High-performance nitrogen photofixation by $\text{Bi}_2\text{Sn}_2\text{O}_7$ nanoparticles enriched with oxygen vacancies

Shuai Gao^{a,1}, Runjie Wu^{a,1}, Mingming Sun^a, Ming Guo^a, Davida Briana DuBois^b,
Shaowei Chen^{b,*}, Haodong Ji^{c,*}, Changzheng Wang^{d,*}, Qiang Wang^{a,*}

^a Laboratory for Micro-sized Functional Materials & College of Elementary Education and Department of Chemistry, Capital Normal University, Beijing 100048, China

^b Department of Chemistry and Biochemistry, University of California, 1156 High Street, Santa Cruz, CA 95064, USA

^c School of Environment and Energy, Peking University Shenzhen Graduate School, Shenzhen, Guangdong 518055, China

^d Beijing Key Laboratory of Functional Materials for Building Structure and Environment Remediation, Beijing University of Civil Engineering and Architecture, Beijing 100044, China

ARTICLE INFO

Keywords:

$\text{Bi}_2\text{Sn}_2\text{O}_7$ nanoparticle
Pyrochlore phase
 O^{2-} -site oxygen vacancy
Photocatalysis
Nitrogen fixation

ABSTRACT

Development of effective technologies for artificial nitrogen fixation under mild conditions is of fundamental and technological significance, as the traditional production of NH_3 by the Haber-Bosch process entails a high energy consumption and carbon emission. In this study, $\text{Bi}_2\text{Sn}_2\text{O}_7$ ultras-small nanoparticles of the pyrochlore phase are synthesized hydrothermally, and the photocatalytic activity towards nitrogen fixation is found to be modulated by the addition of sodium oleate. Among the series, the optimal sample displays a photocatalytic performance with an NH_3 production rate of $231 \mu\text{mol g}^{-1} \text{h}^{-1}$, due to the formation of a high specific surface area, a large number of active sites for N_2 adsorption, and extensive lattice oxygen vacancies. In conjunction with results from first principles calculations, the Bi species around the O^{2-} -site oxygen vacancies are found to play a key role in the adsorption and activation of N_2 . Results from this study highlight the significant potential of $\text{Bi}_2\text{Sn}_2\text{O}_7$ nanostructures as high-performance catalysts for solar ammonia synthesis.

Data Availability: Data will be made available upon request from the authors.

1. Introduction

Ammonia (NH_3) is an important commodity chemical that has found diverse applications, in particular, in agriculture as a fertilizer, and has been produced mostly by the Haber-Bosch procedure [1]. Due to the high dissociation energy of the $\text{N}\equiv\text{N}$ bond (941 kJ mol^{-1}), the fixation of N_2 to NH_3 is energy-intensive requiring high temperatures and pressures ($400\text{--}500^\circ\text{C}$, $100\text{--}200 \text{ atm}$), and the emission of a large amount of greenhouse gases poses significant impacts on the environment [2]. Recently, solar conversion of N_2 into NH_3 has emerged as an environmentally friendly and sustainable technology [3–6]. However, most photocatalysts used for N_2 reduction reaction (NRR) exhibit only a low efficiency of NH_3 production, due to the high recombination of photo-generated electron-hole pairs and limited number of surface active sites [7]. Thus, to enhance the photocatalytic performance, the NRR photocatalysts should exhibit both efficient separation of the electron-hole pairs and enhanced adsorption and activation of N_2 .

Mechanistically, this calls for rational design of the catalytically active sites so as to enhance the interaction between the reactants and photocatalysts, and defect engineering represents a powerful strategy. For instance, the high local electron density of oxygen vacancies (Vo) renders them the viable hotspots for strong interactions with N_2 [7]. This is because oxygen vacancies can facilitate the adsorption of inert $\text{N}\equiv\text{N}$ triple bonds and inject free electrons into π^* antibonding orbitals, which is advantageous to the subsequent N_2 activation process [8,9]. To produce oxygen vacancies, photocatalysts typically undergo thermal treatment at elevated temperatures in a reducing or inert gas atmosphere (i.e., H_2 , Ar or N_2) [10–12]. The processing conditions can be significantly milder with ultrathin photocatalysts, which can be prepared by the addition of structural control agents, and exhibit enhanced N_2 adsorption and activation, due to abundant surface atoms and dangling bonds [7,13]. For instance, Di et al. [14] prepared ultrathin $\text{Bi}_3\text{O}_4\text{Br}$ nanosheets and observed not only improved charge separation but also a positive impact on N_2 adsorption and activation, as compared

* Corresponding authors.

E-mail addresses: shaowei@ucsc.edu (S. Chen), jiahaodong@pku.edu.cn (H. Ji), changzhwang@163.com (C. Wang), qwchem@gmail.com (Q. Wang).

¹ # These authors contributed equally to this work.

to the bulk counterparts. In a recent study [15], we demonstrated that N_2 adsorption and activation, and hence the yield of NH_3 , could be readily improved by adjusting the concentration of oxygen vacancy in ultrafine Bi_5O_7Br nanotubes.

Notably, whereas $Bi_2Sn_2O_7$ has been rather extensively studied due to its polycrystalline phase, the exploration of its catalytic activity has remained limited [16]. The ideal pyrochlore structure of $Bi_2Sn_2O_7$ corresponds to the space group $Fd-3m$ with an intrinsic lattice oxygen vacancy. Such oxygen vacancies can be readily accessible with the formation of an ultrathin structure [17–20]. In addition, the common vertex space structure of $[SnO_6]$ octahedra provides an intrinsic advantage for the separation and transport of electron-hole pairs [21]. In several previous studies, $Bi_2Sn_2O_7$ photocatalysts have been used for pollutant degradation [22,23], CO_2 photoreduction [21], and NH_3 production [24], due to the material's excellent anisotropy and the formation of heterojunctions. For instance, Wu et al. [22] achieved efficient photodegradation of ciprofloxacin (CIP) by constructing $Bi_2Sn_2O_7/MIL-100(Fe)$ nanocomposites. Zhang et al. [23] used $Bi_2Sn_2O_7$ and $BiOBr$ to construct Z-type heterojunctions and achieved advanced oxidative removal of rhodamine b (RhB), tetracycline and CIP under visible light irradiation. It has also been found that the photocatalytic activity of $Bi_2Sn_2O_7$ quantum dots for NH_3 production and CO_2 photoreduction can be modulated by polyvinylpyrrolidone (PVP) [21,24]. In these studies, the harsh reaction conditions (200 °C for 24 h) can lead to the carbonization of the added structural control agents (e.g., PVP and mannitol), thus complicating the structure of the final samples [25–27]. This issue can be mitigated by using a structural control agent that is chemically stable even at high temperatures, and sodium oleate has emerged as a unique candidate [28].

Herein, ultrasmall $Bi_2Sn_2O_7$ nanoparticles (BSO-UNPs) of the pyrochlore phase were rapidly synthesized via a low-temperature hydrothermal procedure using quantitative sodium hydroxide as the mineralizing agent and sodium oleate as the domain-limiting agent. The resultant BSO-UNPs showed a remarkable and stable photocatalytic performance in N_2 fixation under visible light irradiation, at a NH_3 release rate as high as $231 \mu mol g^{-1} h^{-1}$. This was accounted for by the ultrasmall grain size, high dispersion, moderate Vo concentration, and high charge separation efficiency, in excellent agreement with results from density functional theory (DFT) calculations.

2. Experimental section

2.1. Chemicals

All chemicals were of analytical purity and purchased from Shanghai Macklin Biochemicals co., Ltd and used without further purification. Ultrapure water (18 M Ω cm) was used in all experiments.

2.2. Synthesis of ultrasmall $Bi_2Sn_2O_7$ nanoparticles

In a typical experiment, 0.243 g of bismuth nitrate ($Bi(NO_3)_3 \cdot 5 H_2O$) and 0.03 g of sodium oleate were dispersed into 15 mL of 0.1 M mannitol under sonication, into which was slowly injected 5 mL of an aqueous solution of 0.1 M sodium stannate (Na_2SnO_3) to form an opalescent solution, followed by 5 mL of 0.5 M NaOH solution under vigorous stirring. The resultant mixture was transferred to a Teflon-lined autoclave (50 mL) and hydrothermally treated at 160 °C for 12 h. After the reaction, the samples were collected by centrifugation and rinsed with a copious amount of ethanol and water. The obtained sample was denoted as BSO-UNPs.

Four additional samples were prepared in the same manner except that the amount of sodium oleate added was changed to 0.01, 0.1, 0.2 and 0.3 g. The obtained samples were denoted as BSO-X (X = 0.01, 0.1, 0.2, and 0.3).

2.3. Synthesis of bulk $Bi_2Sn_2O_7$

Bulk $Bi_2Sn_2O_7$ was synthesized by employing a high-temperature solid-state reaction method. In brief, 0.46 g of Bi_2O_3 and 0.3 g of SnO_2 were added into 30 mL of ethanol under vigorous stirring to make a homogeneous dispersion. The solid was collected by centrifugation, dried at 80 °C for 5 h, and heated in a crucible at 750 °C in a muffle furnace for 24 h. The resultant sample was referred to as BSO-SSR.

2.4. Structural characterizations

X-ray diffraction (XRD) patterns were acquired with a Shimadzu X-ray diffractometer (XRD-6100) using $Cu K\alpha$ radiation. X-ray photoelectron spectroscopy (XPS) measurements were performed with a Thermo Kratos Axis Supra instrument. All binding energies were calibrated against the C 1s peak at 284.8 eV. Raman spectra were recorded at room temperature using a miniature Raman spectrometer (Horiba) in a backscattered geometry with a 532 nm laser as the excitation source. Electron paramagnetic resonance (EPR) spectra were collected with a Bruker A300 instrument. Brunauer-Emmett-Teller (BET) surface area was analyzed with a Mike ASAP2020 nitrogen sorption device. UV–vis absorption and diffuse reflectance spectroscopy (DRS) measurements were conducted with a Shimadzu UV-2600 UV–visible spectrophotometer. Transmission electron microscopy (TEM) and high-resolution transmission electron microscopy (HRTEM) images were acquired with an electron microscope (USA - FEI-Tecna G2 F20). Nitrogen temperature-programmed desorption (N_2 -TPD) analysis was conducted on a Xianquan-TP5080 instrument (Tianjin, China). Fourier-transform infrared (FTIR) spectra were acquired at room temperature with a Bruker Tensor II FTIR NEXUS spectrometer within the frequency range of 800–4000 cm^{-1} . Steady-state photoluminescence (PL) spectra were collected with an Edinburgh FS5 fluorescence spectrometer.

2.5. Photocatalytic nitrogen fixation

A 300 W Xe lamp was used as the UV–visible light source, and a closed and single-pass N_2 photocatalytic reactor was used as the vessel for fresh NH_4^+ production. The light source was located 15 cm away from the surface of the photocatalyst suspension and provided an intensity of about 2 suns (200 $mW \cdot cm^{-2}$). Typically, 20 mg of a photocatalyst was dispersed uniformly under stirring into 100 mL of ultrapure water. In the dark, N_2 (120 $mL \cdot min^{-1}$) was passed continuously for 1 h to create a pure N_2 environment (positive pressure). The light source was then turned on and an aliquot (5 mL) of the reaction solution was removed every 20 min during the photocatalytic reaction and filtered with a 0.22 μm filter tip. The NH_4^+ in the reaction solution was subsequently detected using a nano reagent (details below).

2.6. Quantitative analysis of NH_4^+ concentration

The NH_4^+ content generated during the photocatalytic nitrogen fixation process was quantified by Nessler's reagent [6]. First, a series of NH_4Cl solutions at different concentrations were prepared, into which was then added potassium sodium tartrate ($KNaC_4H_4O_6$, 0.1 mL, 0.5 mg L^{-1}), followed by Nessler's reagent (0.1 mL) for 10 min's color development. The absorbance at 420 nm was recorded with 0 mg L^{-1} NH_4Cl as the blank calibration, and the standard curve was plotted with NH_4^+ concentration as the x axis and absorbance as the y axis.

2.7. $^{15}N/^{15}NH_4^+$ isotopic labeling

Isotope labeling experiments were performed to identify the source of NH_3/NH_4^+ using $^{15}N_2$ as the feed gas, and the 1H NMR spectra were recorded on a JEOL JNM-ECZ400S NMR spectrometer.

2.8. Electrochemical measurements

Photocurrent response and electrochemical impedance spectroscopy measurements were performed in a three-electrode configuration (CHI 760E, Shanghai, China), where 0.1 M Na₂SO₄ was used as the electrolyte solution, a Pt sheet as the counter electrode, and a saturated calomel electrode (SCE) as the reference electrode. The light source was turned on during the electrochemical impedance spectroscopy. The working electrode was prepared by adding 5 mg of the samples prepared above to 1 mL of ethanol, which was then dropcast onto the surface of an FTO conductive glass electrode with an area of 1 cm × 1 cm after ultrasonic dispersion.

2.9. Quantification of N₂H₄ concentration

N₂H₄ is a common by-product of electrochemical nitrogen reduction reaction. The concentration of N₂H₄ which might be produced in the photocatalytic nitrogen fixation was monitored by spectrophotometric measurements with p-dimethylaminobenzaldehyde as the indicator (color developer), based on the *National Environmental Protection Standard of the People's Republic of China* (HJ 674–2013). Before the experiment, a series of N₂H₄ standard working solutions were prepared at different concentrations, into which was added p-dimethylaminobenzaldehyde. The solution was mixed and allowed to stand for 20 min, and the absorbance at 458 nm (UV-2600, Shimadzu) was recorded to establish a standard curve.

To detect N₂H₄ in the reaction solution, an aliquot (5 mL) of the suspension was removed, into which was added 0.1 mL of concentrated hydrochloric acid (1.19 g mL⁻¹). The solution was then diluted to 10 mL with water to pretreat the clean reaction solution. Thereafter, into 2.5 mL of the treated reaction solution was added 0.5 mL of p-dimethylaminobenzaldehyde. The absorbance at 458 nm was measured after 20 min and compared to the standard curve to estimate the amount of N₂H₄ produced.

2.10. Density functional theory calculations

DFT calculations were conducted using the Cambridge Serial Total Energy Package. The exchange-correlation energy was described using the revised Perdew-Burke-Ernzerhof exchange-correlation density functional (PBESOL) within the generalized-gradient approximation (GGA) [29]. All geometries were fully optimized with a plane-wave kinetic cutoff energy of 400 eV. The Brillouin zone was sampled with 5 × 5 × 5 and 1 × 4 × 1 Monkhorst-Pack k-point grids, respectively, for BSO bulk and (222) surface calculations. A perfect BSO (BSO-SSR) was constructed with 236 atoms (including 28 Bi, 20 Sn and 188 O atoms), and oxygen-vacancy BSO (BSO-UNPs) was constructed with 116 atoms (including 28 Bi, 20 Sn and 187 O atoms). The atomic positions were fully relaxed until a maximum energy difference and residual force on atoms, respectively, converged to 10⁻⁵ eV and 0.03 eV Å⁻¹. A 12 Å thick vacuum layer was used to avoid the interaction between top and bottom surfaces.

The oxygen vacancy formation energy (E_{O-vf}) [30] is defined as $E_{O-vf} = E_{Ov-slab} - E_{slab} + \frac{1}{2}E_{O_2}$, in which E_{slab} is the total electronic energy of a pristine slab, $E_{Ov-slab}$ is the total energy of the slab with surface oxygen vacancy and E_{O_2} is the VASP-sol calculated molecular energy of oxygen in water.

The Gibbs free energy (ΔG) for each photochemical process was calculated according to the following equation [9,31], $\Delta G = \Delta E + E_{ZPE} - T\Delta S$, where ΔE , E_{ZPE} and ΔS denote the changes of DFT energy, zero-point energy and entropy at 298 K, respectively.

3. Results and discussion

3.1. Sample preparation and structural characterizations

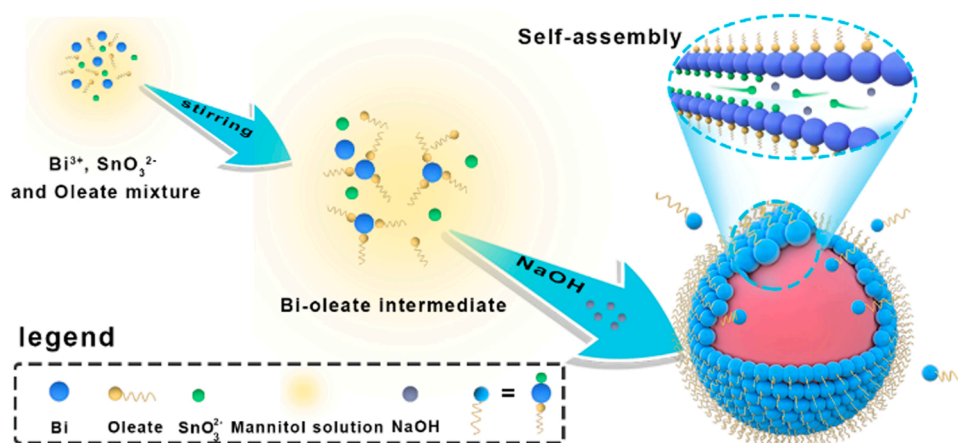
BSO-UNPs of pyrochlore phase were prepared by hydrothermal treatment of a mixed solution containing bismuth nitrate (Bi(NO₃)₃), sodium oleate, sodium stannate (Na₂SnO₃) and sodium hydroxide (NaOH) at 160 °C for 12 h (Scheme 1). Sodium oleate was added to control the growth of Bi₂Sn₂O₇ nanocrystals by forming a passivation layer of Bi-oleate complexes; and for BSO-UNPs the amount added was 0.03 g. Four additional samples were prepared in the same manner but with the addition of a different amount of sodium oleate (X = 0.01, 0.1, 0.2, and 0.3 g) and denoted as BSO-X. Furthermore, bulk Bi₂Sn₂O₇ was synthesized by employing a high-temperature solid-state reaction method and referred to as BSO-SSR.

The materials structures were first characterized by XRD measurements. From the XRD patterns in Fig. 1a, one can see that both BSO-SSR and BSO-UNPs exhibited a series of well-defined diffraction peaks at 2θ = 28.81°, 33.39°, 47.93° and 56.89° that can be assigned to the (222), (400), (440), (622) planes of pyrochlore Bi₂Sn₂O₇ (ICSD #086849), respectively, consistent with the *Fd-3m* space group. Additionally, in comparison to the sharp diffraction patterns of bulk BSO-SSRs, BSO-UNPs can be seen to possess markedly broader peaks with a significantly lower peak intensity, suggesting the formation of ultrasmall-sized nanoparticles and/or increasing disorder. Note that for Bi₂Sn₂O₇ in a typical pyrochlore crystal structure, the symmetrical cubic space group of *Fd-3m* corresponds to the cell parameters of a = b = c = 10.72 Å and a lattice structure consisting of interpenetrating Bi₂O¹ and Sn₂O₆² frameworks and O atoms in two different coordination environments, O¹ (Bi-O-Bi) and O² (Bi-O-Sn) (Fig. 1b).

Further structural insights were obtained in TEM measurements. In contrast to BSO-SSR that exhibited an irregular morphology and consisted of large particles of approximately 200 nm in diameter (Fig. S1), ultrasmall nanoparticles were found in BSO-UNPs with a diameter of only 5.37 nm (Fig. 1c-e). The nanoparticles can be found to exhibit clearly-defined lattice fringes with an interplanar distance of 0.317 nm, consistent with the (222) crystalline planes of pyrochlore Bi₂Sn₂O₇ (ICSD #086849) (Fig. 1f-g). The corresponding selected area electron diffraction (SAED) patterns are shown in Fig. 1h, where four diffraction rings can be identified and assigned to the (222), (400), (440) and (622) planes of pyrochlore Bi₂Sn₂O₇ (ICSD #086849), suggesting good polycrystallinity of the sample. In elemental mapping analysis based on energy-dispersive X-ray (EDX) spectroscopy (Fig. 1i), BSO-UNPs can be seen to exhibit a uniform and overlapping distribution of the Bi, Sn and O elements.

Nitrogen adsorption-desorption measurements were then carried out to examine the sample porosity. From the sorption isotherm (Fig. S2), the Brunauer-Emmett-Teller (BET) specific surface area of BSO-UNPs was estimated to be 484.04 m² g⁻¹, with an average pore diameter of 13.22 nm and average particle diameter of 12.40 nm (Table S1). Note that the latter was qualitatively consistent with the result obtained from HRTEM measurements (Fig. 1e). Such a porous structure in BSO-UNPs is anticipated to provide abundant adsorption sites for N₂ molecules (vide infra). By contrast, BSO-SSR was essentially non-porous, with only a negligible specific surface area (Fig. S2 and Table S1).

The Raman spectra were shown in Fig. 2a and inset, where BSO-SSR exhibited three well-defined peaks at 389, 509 and 529 cm⁻¹, due to the stretching vibrations of Bi-O¹ (F_{1u}), Bi-O² (F_{1u}) and O² (A_{1g}), respectively [17,32], and the peaks at 400 cm⁻¹ (F_{2g}) and 601 cm⁻¹ (F_{2g}) can be ascribed to the Sn-O² vibrations in the Sn₂O₆² framework [33,34]. Notably, the vibrational peaks of BSO-UNPs were drastically broadened and shifted to lower frequencies. Specifically, the two Bi-O² vibration peaks exhibited a red shift to 502 (F_{1u}) and 525 cm⁻¹ (A_{1g}), and Sn-O² to 580 cm⁻¹ (F_{2g}), whereas the Bi-O¹ vibration remained unchanged at 389 cm⁻¹ (F_{1u}). This is consistent with the nanosized particles that contained atomic disorder and crystal defects [17], and suggests that



Scheme 1. Synthesis of ultrasmall $\text{Bi}_2\text{Sn}_2\text{O}_7$ nanoparticles (BSO-UNPs).

oxygen vacancies were most likely generated at the O^2 sites ($\text{O}^2\text{-Vo}$) (Fig. 1b) [34,35].

The surface elemental composition and valence states of the samples were then studied by XPS measurements, where the binding energy was calibrated against the carbon 1s peak of 284.8 eV. From the survey spectra in Fig. 2b, the elements of Bi, Sn, and O can be readily resolved in both BSO-UNPs and BSO-SSR at ca. 163.3, 485.6 and 529.9 eV, respectively. This is consistent with results from EDX elemental mapping analysis (Fig. 1i). The corresponding high-resolution scans of the O 1s electrons are shown in Fig. 2c, where two peaks can be deconvoluted at 529.7 and 531.2 eV, due to lattice oxygen and surface hydroxyl groups, respectively [28,36]. BSO-UNPs exhibited an additional peak at 532.5 eV arising from adsorbed H_2O , likely due to the formation of oxygen vacancies that are known to facilitate H_2O adsorption [37,38].

From the high-resolution scans of the Bi 4f electrons in Fig. 2d, the Bi (III) 4f doublet at 157.9/163.2 eV can be resolved for both BSO-UNPs and BSO-SSR samples [39]; and BSO-UNPs exhibited an additional one at higher energies of 160.6/166.4 eV, suggesting electron depletion of the Bi centers (increasing Bi valence states) [40]. Note that the formation of oxygen vacancies (Bi-Vo) around the Bi(III) sites will produce low-valent $\text{Bi}^{(3-x)+}$ species with a reduced binding energy [39,41]. That is, oxygen vacancies are unlikely to form at the O^1 site. The observed increase in the Bi valence state of BSO-UNPs is therefore likely due to electron transfer to Sn from Bi through the $\text{Bi-O}^2\text{-Sn}$ linkage (Fig. 1b) [40]. Consistent results were obtained from the XPS spectra of the Sn 3d electrons (Fig. 2e), where the Sn(IV) $3d_{5/2}/3d_{3/2}$ doublet can be seen to exhibit a red shift from BSO-SSR (485.8/494.2 eV) to BSO-UNPs (485.4/493.9 eV).

Taken together, results from both the XPS and Raman measurements suggest that oxygen vacancies most likely formed at the O^2 sites. This is further confirmed by results from DFT calculations, where the formation energy of oxygen vacancy was estimated to be ca. 1.462 eV at O^1 and much lower at 0.77 eV at O^2 , suggesting that Bi-Vo-Sn oxygen vacancies are indeed energetically preferred (Fig. 2f-g).

The formation of oxygen vacancies was indeed confirmed in EPR measurements. For the BSO-UNPs sample (Fig. 2h), a strong EPR signal is observed at $g = 1.93$, which is consistent with the capture of electrons by oxygen vacancies in SnO_2 [42,43]. By contrast, the signal was markedly weaker with BSO-SSR, which, in conjunction with the BET results, suggests that the oxygen vacancies mostly resided in the interior of the materials. This may be facilitated by the ultra-small size of the nanoparticles, rampant disorder, as well as low atomic escape energy on the surface of the sample. Significantly, the $\text{O}^2\text{-Vo}$ in BSO-UNPs may serve as effective sites to capture photoelectrons and suppress recombination of charge carriers (Fig. 2i), as observed below.

3.2. Photocatalytic reduction of nitrogen

The photocatalytic performance towards nitrogen fixation to ammonia was then evaluated and compared by using a 300 W xenon lamp as the light source without any co-catalyst or sacrificial agent. The produced NH_4^+ was detected and quantified by the Nessler's reagent chromogenic method, with the calibration curve shown in Fig. S3 and Table S2. From Fig. 3a, it can be seen that BSO-UNPs exhibited a significantly enhanced photocatalytic performance towards nitrogen fixation, as compared to BSO-SSR, with a NH_4^+ yield of $178.34 \mu\text{mol g}^{-1}$ in 1 h and a maximum ammonia production rate of $231 \mu\text{mol g}^{-1} \text{h}^{-1}$. By contrast, virtually no NH_4^+ was detected with BSO-SSR. In addition, no ammonia was produced in the dark or under Ar purging, indicating that the ammonia detected was produced solely from the photocatalytic nitrogen fixation (Fig. 3b). To further confirm that N_2 was the only source of conversion to NH_3 , we performed ^{15}N isotopic labeling experiments using $^{15}\text{N}_2$ as the feed gas, and $^{15}\text{NH}_4^+$ was the only detectable product in ^1H NMR measurements (Fig. 3c) [44].

Notably, the catalytic activity varied markedly with the amounts (X) of sodium oleate added in sample preparation, first increasing and then decreasing with X, with BSO-UNPs standing out as the best catalyst among the series (Fig. 3b). Yet in XRD measurements (Fig. S4), the diffraction patterns were essentially the same among the samples, indicating minimal impacts of the amount of sodium oleate added on the crystal form of bismuth stannate. In TEM measurements (Fig. S5), however, one can see that with increasing X, agglomeration of BSO nanoparticles became gradually intensified. In addition, EPR measurements showed that the oxygen vacancy concentration increased with the increasing amount of sodium oleate added (Fig. S6), where the excessive surface Vo and thus the formation of carrier complex centers were likely responsible for the decrease of the catalytic activity [5]. Consistent results were obtained in photoluminescence (PL) measurements, where BSO-UNPs exhibited the lowest emission intensity among the series, suggesting maximal efficiency of the separation of photogenerated electron-hole pairs (Fig. S7). Taken together, these results demonstrate that BSO-UNPs, which was prepared with the addition of 0.03 g of sodium oleate, represents the optimal structure for photocatalytic ammonia synthesis due to moderate dispersion and Vo concentration.

The stability of the catalysts was then tested by a long-term assay of photocatalytic ammonia synthesis for 8 h and in four cycles (Fig. 3d-e). After 8 h's photocatalytic reaction (Fig. 3c), the amount of ammonia produced was estimated to be 1.36 mmol g^{-1} at a production rate of $170.1 \mu\text{mol g}^{-1} \text{h}^{-1}$, which was consistent with that obtained earlier at 1 h (Fig. 3a). Note that the crystal structure, morphology and Vo concentration of BSO-UNPs showed practically no change after 8 h's photocatalytic reaction, as confirmed by XRD, TEM and EPR measurements (Fig. S8-S10). Additionally, after four cycles of testing, the ammonia

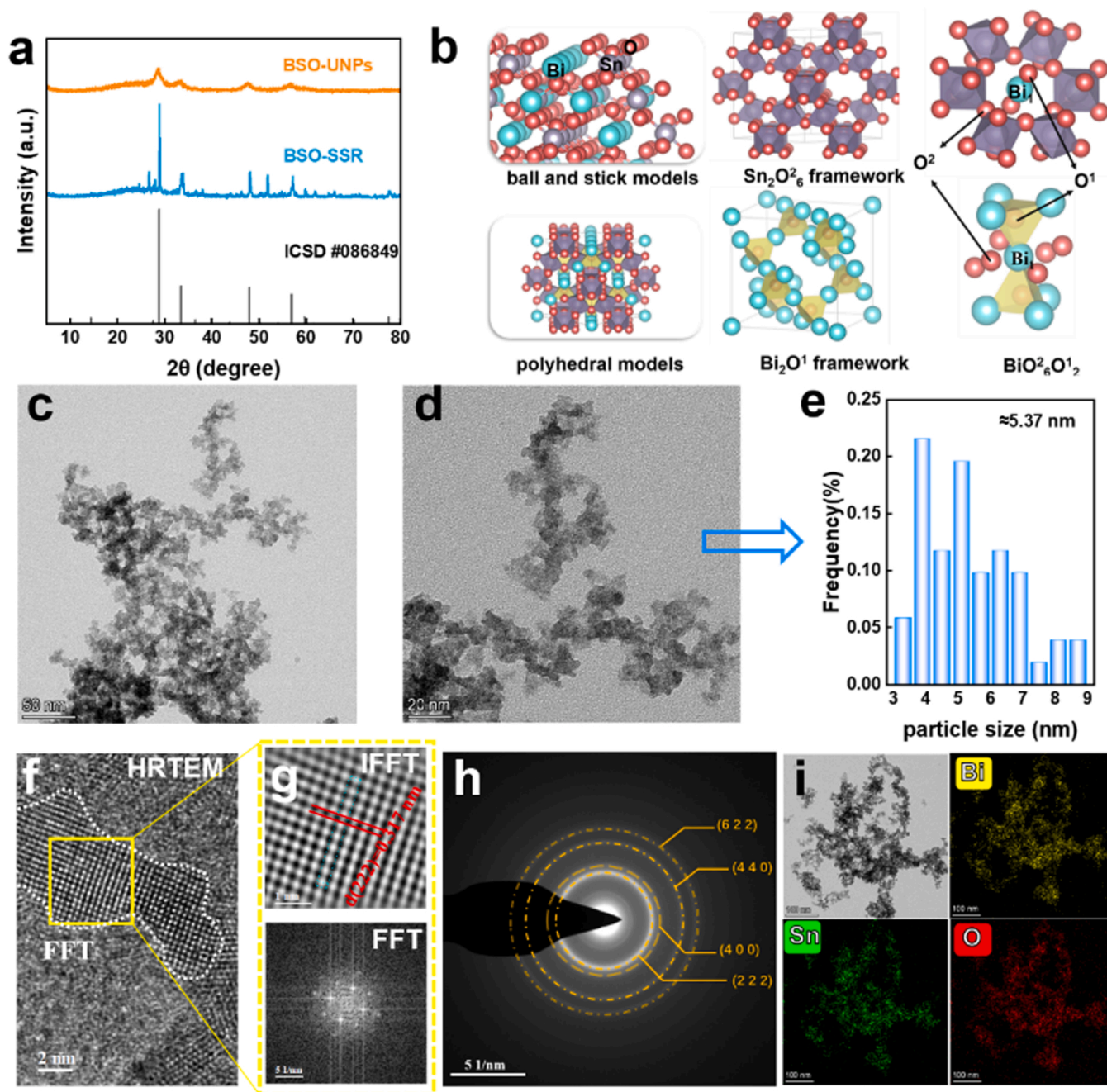


Fig. 1. (a) XRD patterns of BSO-UNPs and BSO-SSR. (b) Crystal structure diagram of pyrochlore $\text{Bi}_2\text{Sn}_2\text{O}_7$. (c, d) TEM images, (e) nanoparticle size distribution, (f) TEM image and (g) the corresponding IFFT and FFT patterns, (h) SAED patterns, and (i) EDX-based elemental maps of BSO-UNPs.

release rate remained essentially invariant (Fig. 3e). Remarkably, no N_2H_4 was detected during the photocatalytic reaction (Figs. S11–S12, Table S3), indicating the high selectivity of BSO-UNPs for NH_3 synthesis. Significantly, BSO-UNPs outperformed a large number of Bi-based photocatalysts reported previously for photocatalytic nitrogen fixation (Fig. 3f and Table S4).

To gain insights into the photocatalytic activity of BSO-UNPs, the adsorption properties of N_2 molecules onto the surface of BSO-UNPs were first examined using DFT calculations. In the calculations, the N_2 molecule was rotated laterally for the bidentate Bi–N=N–Sn adsorption (Fig. 4a). Yet, the =N–Sn linkage became disconnected during structural relaxation; and at the end of structural optimization, the N_2 molecule was actually bonded to the Bi atom near the O^2 -Vo site (Fig. 4b). The adsorption energy of N_2 molecules on BSO-SSR (pristine BSO) and BSO-

UNPs were then computed and compared (Fig. 4c), where one can see that the N_2 adsorption energy is higher on BSO-SSR (−1.624 eV) than on BSO-UNPs (−0.120 eV). This is consistent with results from temperature-programmed nitrogen desorption (N_2 -TPD) assay. It can be seen from Fig. 4d that a single desorption peak appeared at ca. 103 °C for BSO-SSR, due to physisorbed N_2 [45], whereas for BSO-UNPs, the N_2 desorption occurred at a much higher temperature (ca. 420 °C), suggestive of chemisorption of the N_2 molecules [46]. Note that chemical adsorption involves electron transfer between the N_2 molecules and the photocatalyst, leading to activation of molecular nitrogen, a critical first step in NRR [45,47]. In addition, it has been demonstrated that oxygen vacancies at the O^2 site may facilitate photogenerated charge transfer [35].

The BSO-SSR sample exhibited a dark yellow color, whereas BSO-

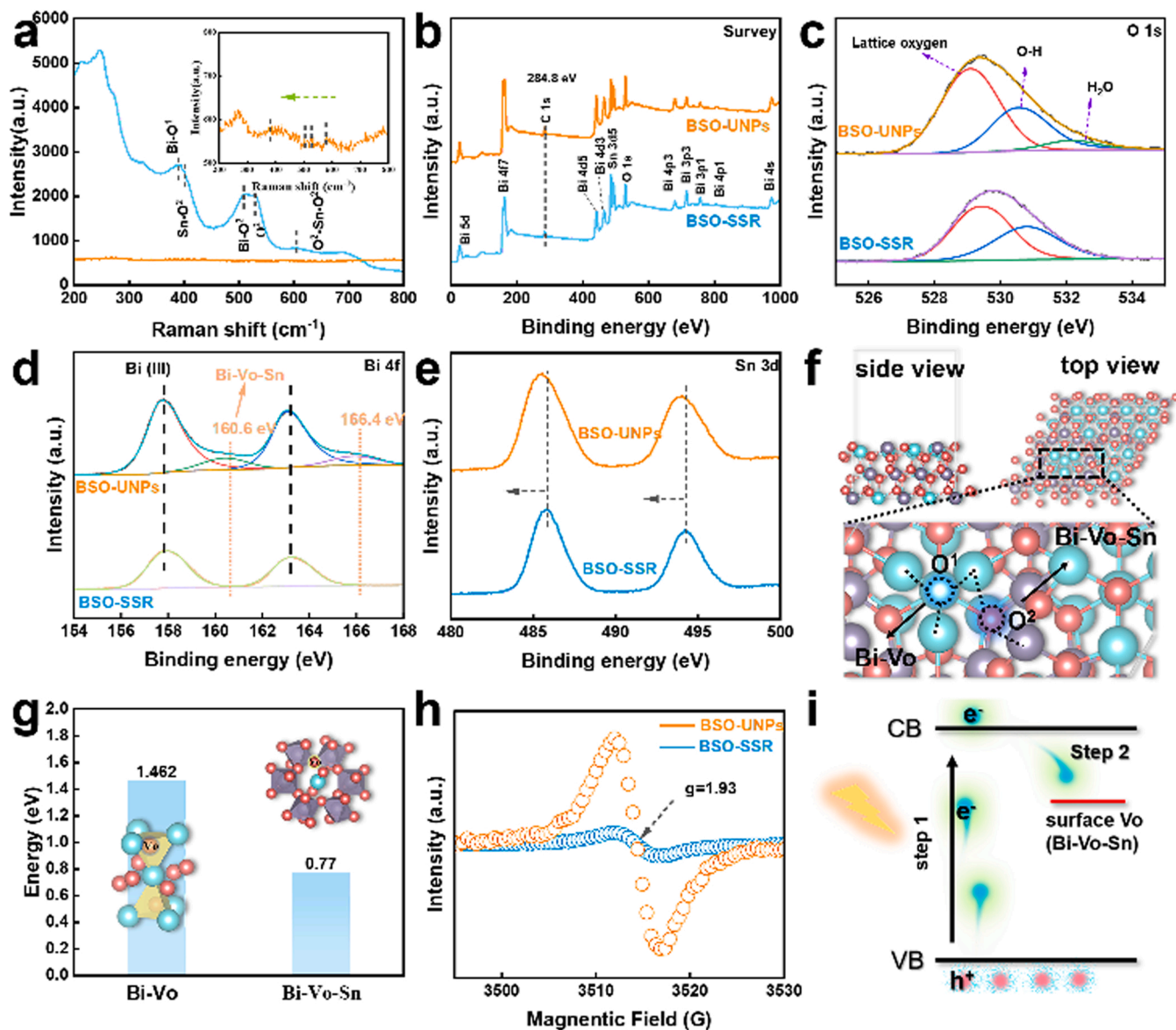


Fig. 2. (a) Raman spectra (inset is the zoom in of the BSO-UNPs sample), (b) XPS survey spectra, and high-resolution scans of the (c) O 1s, (d) Bi 4f and (e) Sn 3d electrons of BSO-UNPs and BSO-SSR. (f) Diagram of the generation of oxygen vacancies at the O¹ (O¹-Vo, Bi-Vo) and O² (O²-Vo, Bi-Vo-Sn) sites, with the corresponding vacancy generation energies shown in (g). (h) EPR spectra of BSO-SSR and BSO-UNPs. (i) Schematic diagram of the migration of photogenerated carriers.

NPs was gray-black. In UV-vis diffuse reflectance spectroscopy (DRS) measurements (Fig. S13a), BSO-SSR can be seen to exhibit no absorption beyond 500 nm, which is consistent with its forbidden bandgap of ca. 2.41 eV (Fig. S13b). For comparison, due to the formation of surface oxygen vacancies, BSO-UNPs exhibited a markedly stronger absorption in the visible range, with a somewhat reduced bandgap of 2.27 eV. According to the XPS valence band (VB) spectra (Fig. S13c), the VB of BSO-SSRs and BSO-NPs was estimated to be 1.1 and 0.76 eV, respectively. Therefore, the corresponding conduction band (CB) was calculated to be -1.31 and -1.54 eV (Fig. S13d). The formation of oxygen vacancies led to new defect states within the band gap and hence an upward shift of the Fermi level. This facilitated the absorption in the visible range, separation of photogenerated electron-hole pairs, and the eventual photocatalytic N₂ reduction for NH₃ synthesis [21,24,48].

From the Nyquist plot of electrochemical impedance spectroscopy measurements (Fig. 4e), the BSO-UNPs sample can be seen to exhibit a clearly smaller arc radius, suggesting a lower charge-transfer resistance (R_{CT}), than BSO-SSR. Consistent results were obtained in transient photocurrent response tests (TPCR) under UV-visible photoirradiation

(Fig. 4e inset), where BSO-UNPs possessed significantly higher photocurrents than BSO-SSR, suggesting far more efficient separation of the photogenerated electron-hole pairs. This is further confirmed in steady-state PL measurements (Fig. 4f), where BSO-UNPs exhibited a drastically lower emission intensity than BSO-SSR (under 360 nm excitation). For the nanosized BSO-UNPs, the photogenerated carriers were more likely to migrate from the interior to the surface of the sample under photoexcitation, and Vo as a surface defect could facilitate the trapping of electrons, increase carrier lifetime and hence improve charge separation efficiency [28].

3.3. Mechanistic study

To further understand the nitrogen fixation mechanism, in situ FTIR experiments were conducted to investigate the adsorption and activation of nitrogen on the BSO-UNPs surface (Fig. 5a). A drop of water was placed onto the sample to retain the actual photocatalytic environment, and then a large amount of argon and N₂ was pumped in to establish a saturated N₂ atmosphere, before spectral data were acquired at 5 min

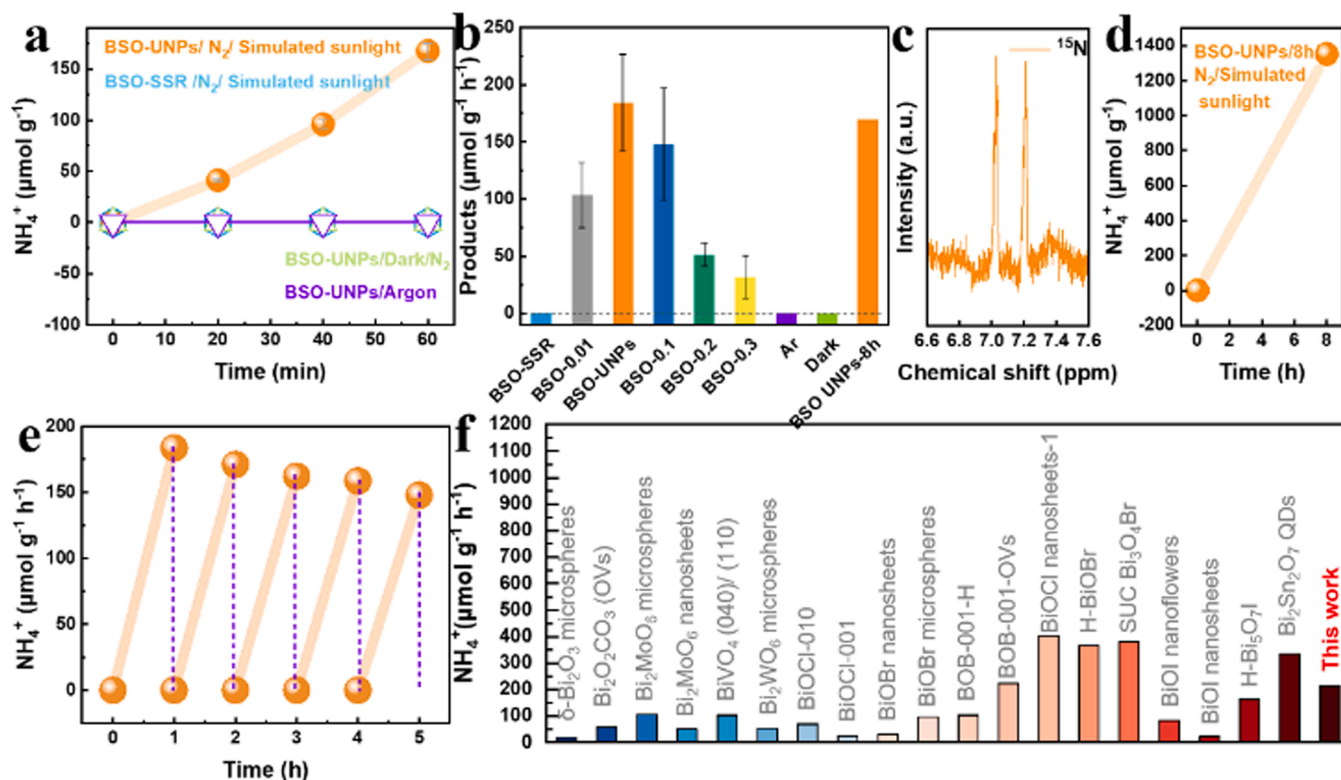


Fig. 3. (a) Photocatalytic ammonia production by BSO-SSR and BSO-UNPs. (b) Photocatalytic ammonia release rates of BSO-SSR, BSO-UNPs, BSO-X (X = 0.01, 0.1, 0.2 and 0.3) and control experiments (in the dark and under Ar purging). (c) ^{15}N NMR spectrum of $^{15}\text{NH}_4^+$ produced by NRR. (d) Long-term test of photocatalytic nitrogen fixation and (e) cycling test data of BSO-UNPs. (f) Comparison of the catalytic performance of BSO-UNPs with relevant bismuth-based catalysts reported previously in the literature. The NH_3 release rate, ammonia concentration and other details are summarized in Table S4.

intervals during photo illumination of the sample. Fig. 5b shows the corresponding FTIR spectra of N_2 fixation for up to 30 min's photo-irradiation, in which a series of vibrational bands can be clearly identified, peak i (3580 cm^{-1}) due to the stretching vibration of N-H [15], peak ii (2882 cm^{-1}) and peak v (1403 cm^{-1}) both the characteristic stretching vibrations of adsorbed NH_4^+ [49], peak iii (1714 cm^{-1}) the characteristic stretching vibration of adsorbed NH_3 [50], and peak iv (1675 cm^{-1}) due to chemisorbed N_2 molecules [51]. Furthermore, one can see that with prolonged reaction time, peaks i, ii and v are significantly enhanced in intensity, while peaks iii and iv are markedly diminished, indicating an enhanced conversion of N_2 to NH_4^+ that is adsorbed on the surface of BSO-UNPs ($\text{N}_2 \rightarrow \text{NH}_3 \rightarrow \text{NH}_4^+$). Notably, the two characteristic vibrations of N_2H_4 at 1290 cm^{-1} and 1129 cm^{-1} were not observed, suggesting that subsequent nitrogen fixation follows a distal pathway [30,52].

The Gibbs free energy of nitrogen reduction on BSO-SSR and BSO-UNPs was then computed using DFT calculations to evaluate the influence of the ligand environment around the O^{2-} site vacancies on the activation of N_2 (Fig. 5c). In the reduction of N_2 to NH_3 , the first hydrogenation step is the protonation of N_2 to N-NH ($\text{N}_2 + \text{H}^+ \rightarrow \text{N-NH}$), which is a potential limiting step in the overall N_2 fixation process [30]. This has to overcome the high free energy barrier of 2.336 eV for BSO-SSR, but only requires an input energy of 0.802 eV for BSO-UNPs. In the subsequent hydrogenation step ($\text{N-NH}_2 + \text{H}^+ \rightarrow \text{N-NH}_3$), the energy required for BSO-UNPs remains lower (1.092 eV) than for BSO-SSR (1.552 eV). For BSO-UNPs, the subsequent step of N-NH_3 desorption to N is mainly an exothermic process. It is noteworthy that both BSO-SSR and BSO-UNPs show a high free energy barrier during N-NH_3 desorption. Although this process is endothermic, the protonation of N-NH_3 to NH_4^+ in solution is a favorable step [53]. In conclusion, after N_2 is chemisorbed onto the surface of BSO-UNPs, the thermodynamic barrier for N_2 reduction is markedly lowered, thereby facilitating the

continuous activation of N_2 molecules. Consistent results were obtained from the corresponding N-N bond lengths (Fig. 5d), which varied in the order of free N_2 molecule (1.078 \AA) < N_2 (1.170 \AA) < N-NH (1.277 \AA) < N-NH_2 (1.332 \AA) < N-NH_3 (1.450 \AA), suggesting the continuous activation of N_2 molecules at the O^{2-} vacancy on the BSO-UNPs surface.

The protonation process of N_2 molecules on the surface of BSO-UNPs was then investigated by the calculations of partial wave density of states (PDOS). With the continuous activation of the N_2 molecule (Fig. 5e-g), the electronic state of the N 2p orbital continues to be strongly split, and the electron transfer between the N_2 molecule and the surface Vo reaches an equilibrium, which suggests injection of photo-generated electrons into the π^* antibonding orbitals of N_2 , thereby facilitating N_2 activation and subsequent protonation reactions. After the protonation of N_2 to N-NH , the electronic state of Bi undergoes a significant decrease, while the electronic state of Sn does not change much, implying that the photogenerated electrons are transferred to the π^* antibonding orbital of the N_2 molecule via the Bi-Vo path. From the electron density (ED) and electron density difference (EDD) images (Fig. 5 h), it can be seen that the electron transfer and enrichment between Bi-Vo and N_2 molecules (Bi-Vo-N=N bonding mechanism) is significant, consistent with the variation of the N≡N bond length, indicating that the O^{2-} site vacancies on the surface of BSO-UNPs indeed play a crucial role in N_2 activation.

Therefore, the drastically enhanced photocatalytic activity of BSO-UNPs can be accounted for by the following factors. (a) The nanosized structure led to a significant increase of the specific surface area, which facilitated the escape of oxygen atoms from the sample surface generating structural defects, as well as migration of oxygen vacancies from the sample interior to the surface providing a large number of anchor points for the adsorption of N_2 molecules. (b) Upon adsorption onto the oxygen vacancies on the BSO-UNPs surface, N_2 molecules were continuously activated by electrons and H^+ species, due to efficient charge

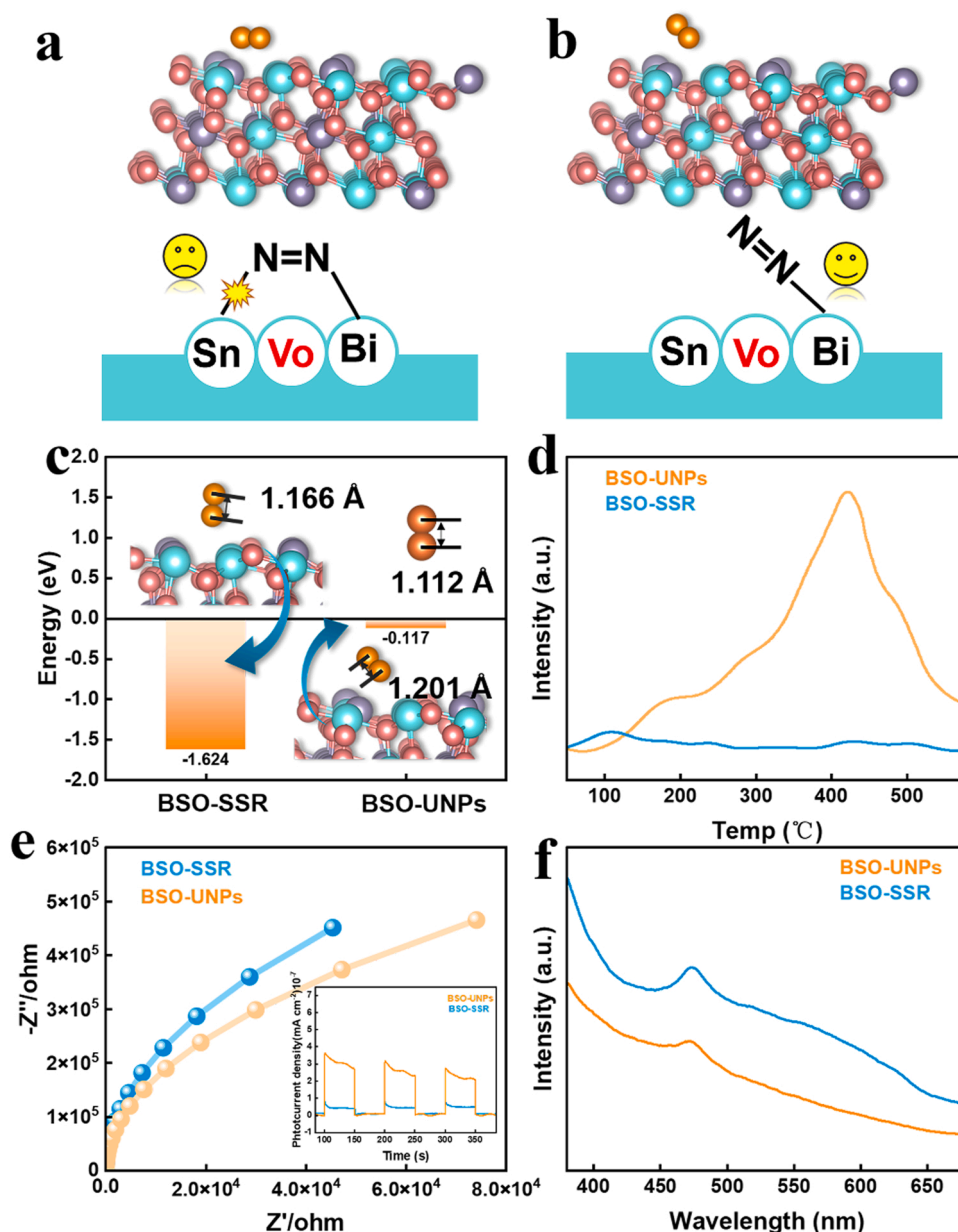


Fig. 4. (a, b) Structural models of nitrogen adsorption on the O^2 site on the BSO-UNPs surface. (c) N_2 adsorption energy on BSO-SSR and BSO-UNPs. (d) N_2 -TPD, (e) Nyquist plots (inset is the periodic on/off photocurrent responses) and (f) photoluminescence emission spectra of BSO-SSR and BSO-UNPs under 360 nm excitation.

separation of BSO-UNPs, and the Bi species would activate $\text{N}\equiv\text{N}$ by injecting electrons into the π^* antibonding orbital ($\text{Bi-Vo-N}=\text{N}$). (c) NH_3 was not detected with BSO-SSR, as the oxygen vacancies were mostly confined within the sample interior making minimal contributions to N_2 adsorption and activation [54]. Therefore, it is believed that the Bi species adjacent to Vo were the primary active centers for N_2 photocatalytic nitrogen fixation to ammonia.

4. Conclusion

In this study, ultrasmall $\text{Bi}_2\text{Sn}_2\text{O}_7$ nanoparticles (BSO-UNPs) of the pyrochlore phase rich in oxygen vacancies were synthesized by a facile hydrothermal procedure with the addition of a different amount of sodium oleate. Compared with bulk $\text{Bi}_2\text{Sn}_2\text{O}_7$ that was prepared by a high-temperature solid-state reaction (BSO-SSR), BSO-UNPs exhibited a markedly enhanced photocatalytic activity towards the nitrogen fixation to ammonia, due to the formation of surface defects that facilitated the adsorption and activation of N_2 molecules. In situ spectroscopic

measurements and DFT calculations suggested that the Bi centers adjacent to surface oxygen defects served as the active sites for photocatalytic N_2 fixation ($\text{Bi-Vo-N}=\text{N}$). Results from this work highlight the significance of defect engineering in the development of high-performance, low-cost photocatalysts for artificial nitrogen fixation.

CRediT authorship contribution statement

Shuai Gao: Data curation, Formal analysis, Writing – original draft. **Runjie Wu:** Data curation, Formal analysis, Writing – original draft. **Ming Guo:** Data curation, Formal analysis. **Mingming Sun:** Data curation, Formal analysis. **David Briana DuBois:** Formal analysis, Writing – review & editing. **Haodong Ji:** Formal analysis, Writing – review & editing. **Changzheng Wang:** Formal analysis, Writing – review & editing. **Qiang Wang:** Conceptualization, Methodology, Formal analysis, Funding acquisition, Writing – original draft. **Shaowei Chen:** Formal analysis, Resources, Writing – review & editing.

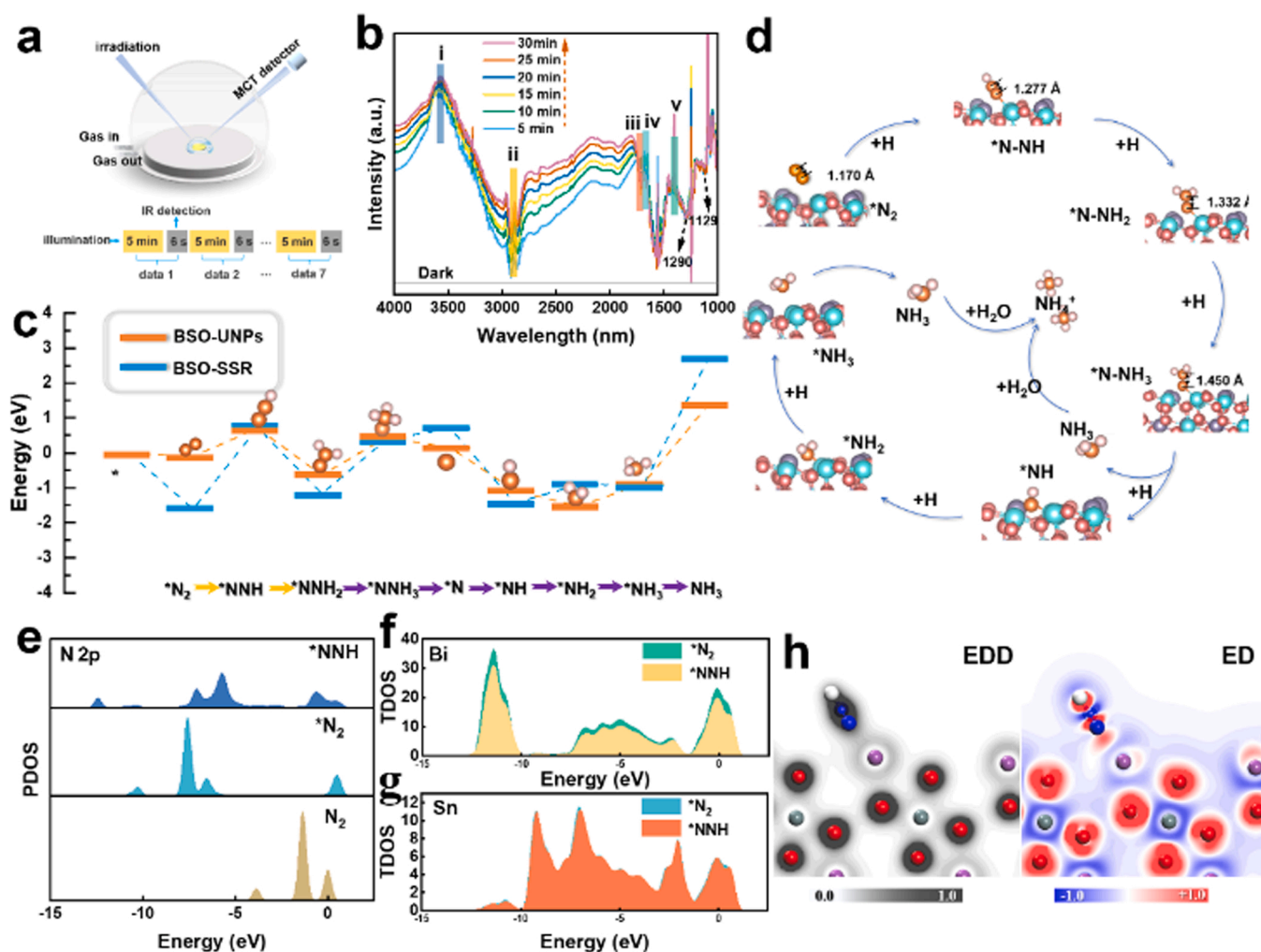


Fig. 5. (a) Schematic diagram of the in-situ FTIR setup. (b) In situ FTIR spectra of N_2 fixation on BSO-UNPs for up to 30 min's photoirradiation. (c) Reaction energy diagram of nitrogen fixation photocatalyzed by BSO-SSR and BSO-UNPs. (d) NRR pathway on the O^2 site. TDOS of (e) Bi and (f) Sn and (g) the corresponding PDOS of N 2p at $*N_2$ and $*N-NH$ steps on BSO-UNPs. (h) Electron density (ED) and electron density difference (EDD) images of N_2 molecule protonation ($*N-NH$) during photocatalytic synthesis of NH_3 by BSO-UNPs, where red represents electron gain, and blue represents electron loss.

Declaration of Competing Interest

The authors declare that they have no known competing financial interests or personal relationships that could have appeared to influence the work reported in this paper.

Data availability

Data will be made available on request.

Acknowledgments

This work was supported by the National Natural Science Foundation of China (52100069 and 21471103). S.W.C. thanks the National Science Foundation for partial support of the work (CBET-1848841 and CHE-2003685).

Appendix A. Supporting information

Supplementary data associated with this article can be found in the online version at [doi:10.1016/j.apcatb.2022.122260](https://doi.org/10.1016/j.apcatb.2022.122260).

References

- [1] H. Li, M. Xia, B. Chong, H. Xiao, B. Zhang, B. Lin, B. Yang, G. Yang, Boosting photocatalytic nitrogen fixation via constructing low-oxidation-state active sites in the nanoconfined spinel iron cobalt oxide, *ACS Catal.* 12 (2022) 10361–10372.
- [2] M. Li, H. Huang, J. Low, C. Gao, R. Long, Y. Xiong, Recent progress on electrocatalyst and photocatalyst design for nitrogen reduction, *Small Methods* 3 (2019) 1800388.
- [3] S. Zhang, Y. Zhao, R. Shi, C. Zhou, G.I.N. Waterhouse, Z. Wang, Y. Weng, T. Zhang, Sub-3 nm Ultrafine Cu_2O for Visible Light Driven Nitrogen Fixation, *Angew. Chem. Int. Ed.* 60 (2021) 2554–2560.
- [4] T. Wang, J. Liu, P. Wu, C. Feng, D. Wang, H. Hu, G. Xue, Direct Utilization of Air and Water as Feedstocks in the Photo-driven Nitrogen Reduction Reaction over a Ternary Z-scheme $SiW_9Co_3/PDA/BWO$ Hetero-junction, *J. Mater. Chem. A* 8 (2020) 16590–16598.
- [5] Z. Zhao, D. Wang, R. Gao, G. Wen, M. Feng, G. Song, J. Zhu, D. Luo, H. Tan, X. Ge, W. Zhang, Y. Zhang, L. Zheng, H. Li, Z. Chen, Magnetic-Field-Stimulated Efficient Photocatalytic N_2 Fixation over Defective $BaTiO_3$ Perovskites, *Angew. Chem. Int. Ed.* 60 (2021) 11910–11918.
- [6] P. Yang, R. Zhao, J. Liu, T. Wang, C. Feng, H. Hu, G. Xue, Designing “Core-Shell” Insoluble- $SiW_{11}Fe@6-Bi_2O_3$ Z-Scheme Heterojunction for Photo-Driven Nitrogen Reduction Reaction and Evaluating the Impact of Oxygen toward Nitrogen Reduction, *Adv. Mater. Interfaces* 9 (2022) 2102031.
- [7] J. Xiong, P. Song, J. Di, H. Li, Atomic-level active sites steering in ultrathin photocatalysts to trigger high efficiency nitrogen fixation, *Chem. Eng. J.* 402 (2020), 126208.
- [8] Y. Bo, H. Wang, Y. Lin, T. Yang, R. Ye, Y. Li, C. Hu, P. Du, Y. Hu, Z. Liu, R. Long, C. Gao, B. Ye, L. Song, X. Wu, Y. Xiong, Altering hydrogenation pathways in photocatalytic nitrogen fixation by tuning local electronic structure of oxygen vacancy with dopant, *Angew. Chem. Int. Ed.* 60 (2021) 16085–16092.

- [9] Y. Zhao, Y. Zhao, R. Shi, B. Wang, G.I.N. Waterhouse, L.-Z. Wu, C.-H. Tung, T. Zhang, Tuning Oxygen Vacancies in Ultrathin TiO_2 Nanosheets to Boost Photocatalytic Nitrogen Fixation up to 700 nm, *Adv. Mater.* 31 (2019) 1806482.
- [10] H. Yu, F. Chen, X. Li, H. Huang, Q. Zhang, S. Su, K. Wang, E. Mao, B. Mei, G. Mul, T. Ma, Y. Zhang, Synergy of Ferroelectric Polarization and Oxygen Vacancy to Promote CO_2 Photoreduction, *Nat. Commun.* 12 (2021) 4594.
- [11] C. Wang, F. Chen, C. Hu, T. Ma, Y. Zhang, H. Huang, Efficient Piezocatalytic H_2O_2 Production of Atomic-level Thickness $\text{Bi}_4\text{Ti}_3\text{O}_{12}$ Nanosheets with Surface Oxygen Vacancy, *Chem. Eng. J.* 431 (2022), 133930.
- [12] H. Zheng, X. Li, K. Zhu, P. Liang, M. Wu, Y. Rao, R. Jian, F. Shi, J. Wang, K. Yan, J. Liu, Semiconducting BaTiO_3/C Core-shell Structure for Improving Piezo-photocatalytic Performance, *Nano Energy* 93 (2022), 106831.
- [13] J. Xiong, P. Song, J. Di, H. Li, Ultrathin structured photocatalysts: a versatile platform for CO_2 reduction, *Appl. Catal., B* 256 (2019), 117788.
- [14] J. Di, J. Xia, M.F. Chisholm, J. Zhong, C. Chen, X. Cao, F. Dong, Z. Chi, H. Chen, Y.-X. Weng, J. Xiong, S.-Z. Yang, H. Li, Z. Liu, H. Dai, Defect-Tailoring Mediated Electron-Hole Separation in Single-Unit-Cell $\text{Bi}_3\text{O}_5\text{Br}$ Nanosheets for Boosting Photocatalytic Hydrogen Evolution and Nitrogen Fixation, *Adv. Mater.* 31 (2019) 1807576.
- [15] P. Li, Z. Zhou, Q. Wang, M. Guo, S. Chen, J. Low, R. Long, W. Liu, P. Ding, Y. Wu, Y. Xiong, Visible-Light-Driven Nitrogen Fixation Catalyzed by $\text{Bi}_5\text{O}_7\text{Br}$ Nanostructures: Enhanced Performance by Oxygen Vacancies, *J. Am. Chem. Soc.* 142 (2020) 12430–12439.
- [16] X. Feng, J. Xu, X. Xu, S. Zhang, J. Ma, X. Fang, X. Wang, Unraveling the Principles of Lattice Disorder Degree of $\text{Bi}_2\text{B}_2\text{O}_7$ ($\text{B} = \text{Sn}, \text{Ti}, \text{Zr}$) Compounds on Activating Gas Phase O_2 for Soot Combustion, *ACS Catal.* 11 (2021) 12112–12122.
- [17] J. Xu, Y. Zhang, X. Xu, X. Fang, R. Xi, Y. Liu, R. Zheng, X. Wang, Constructing $\text{La}_2\text{B}_2\text{O}_7$ ($\text{B} = \text{Ti}, \text{Zr}, \text{Ce}$) Compounds with Three Typical Crystalline Phases for the Oxidative Coupling of Methane: The Effect of Phase Structures, Superoxide Anions, and Alkalinity on the Reactivity, *ACS Catal.* 9 (2019) 4030–4045.
- [18] J.W. Lewis, J.L. Payne, I.R. Evans, H.T. Stokes, B.J. Campbell, J.S.O. Evans, An exhaustive symmetry approach to structure determination: phase transitions in $\text{Bi}_2\text{Sn}_2\text{O}_7$, *J. Am. Chem. Soc.* 138 (2016) 8031–8042.
- [19] J. Di, C. Zhu, M. Ji, M. Duan, R. Long, C. Yan, K. Gu, J. Xiong, Y. She, J. Xia, H. Li, Z. Liu, Defect-rich $\text{Bi}_{12}\text{O}_{17}\text{Cl}_2$ nanotubes self-accelerating charge separation for boosting photocatalytic CO_2 reduction, *Angew. Chem. Int. Ed.* 57 (2018) 14847–14851.
- [20] J. Di, C. Chen, S.-Z. Yang, M. Ji, C. Yan, K. Gu, J. Xia, H. Li, S. Li, Z. Liu, Defect engineering in atomically-thin bismuth oxychloride towards photocatalytic oxygen, *Evol., J. Mater. Chem. A* 5 (2017) 14144–14151.
- [21] S. Guo, J. Di, C. Chen, C. Zhu, M. Duan, C. Lian, M. Ji, W. Zhou, M. Xu, P. Song, R. Long, X. Cao, K. Gu, J. Xia, H. Liu, Y. Zhao, L. Song, Y. Xiong, S. Li, Z. Liu, Oxygen Vacancy Mediated Bismuth Stannate Ultra-small Nanoparticle towards Photocatalytic CO_2 -to- CO Conversion, *Appl. Catal., B* 276 (2020), 119156.
- [22] C. Wu, Q. Shen, S. Zheng, X. Zhang, J. Sheng, H. Yang, Fabrication of $\text{Bi}_2\text{Sn}_2\text{O}_7$ @ MIL-100(Fe) Composite Photocatalyst with Enhanced Superoxide-radical-dominated Photocatalytic Activity for Ciprofloxacin, *Degrad., J. Mol. Struct.* 1258 (2022), 132657.
- [23] D. Zhang, M. Wu, J. Hao, S. Zheng, Y. Yang, T. Yao, Y. Wang, Construction of Z-scheme Heterojunction by Coupling $\text{Bi}_2\text{Sn}_2\text{O}_7$ and BiOBr with Abundant Oxygen Vacancies: Enhanced Photodegradation Performance and Mechanism Insight, *J. Colloid Interface Sci.* 612 (2022) 550–561.
- [24] Y. Zhang, J. Di, X. Qian, M. Ji, Z. Tian, L. Ye, J. Zhao, S. Yin, H. Li, J. Xia, Oxygen vacancies in $\text{Bi}_2\text{Sn}_2\text{O}_7$ quantum dots to trigger efficient photocatalytic nitrogen reduction, *Appl. Catal., B* 299 (2021), 120680.
- [25] S. Gao, B. Gu, X. Jiao, Y. Sun, X. Zu, F. Yang, W. Zhu, C. Wang, Z. Feng, B. Ye, Y. Xie, Highly Efficient and Exceptionally Durable CO_2 Photoreduction to Methanol over Freestanding Defective Single-Unit-Cell Bismuth Vanadate Layers, *J. Am. Chem. Soc.* 139 (2017) 3438–3445.
- [26] J. Wu, X. Li, W. Shi, P. Ling, Y. Sun, X. Jiao, S. Gao, L. Liang, J. Xu, W. Yan, C. Wang, Y. Xie, Efficient Visible-Light-Driven CO_2 Reduction Mediated by Defect-Engineered BiOBr Atomic Layers, *Angew. Chem. Int. Ed.* 57 (2018) 8719–8723.
- [27] M. Guan, C. Xiao, J. Zhang, S. Fan, R. An, Q. Cheng, J. Xie, M. Zhou, B. Ye, Y. Xie, Vacancy associates promoting solar-driven photocatalytic activity of ultrathin bismuth oxychloride nanosheets, *J. Am. Chem. Soc.* 135 (2013) 10411–10417.
- [28] L. Liu, H. Huang, F. Chen, H. Yu, N. Tian, Y. Zhang, T. Zhang, Cooperation of Oxygen Vacancies and 2D Ultrathin Structure Promoting CO_2 Photoreduction Performance of $\text{Bi}_4\text{Ti}_3\text{O}_{12}$, *Sci. Bull.* 65 (2020) 934–943.
- [29] J.P. Perdew, A. Ruzsinszky, G.I. Csonka, O.A. Vydrov, G.E. Scuseria, L. A. Constantin, X. Zhou, K. Burke, Restoring the Density-Gradient Expansion for Exchange in Solids and Surfaces, *Phys. Rev. Lett.* 100 (2008), 136406.
- [30] Xa Dong, Z. Cui, X. Shi, P. Yan, Z. Wang, A.C. Co, F. Dong, Insights into Dynamic Surface Bromide Sites in $\text{Bi}_4\text{O}_5\text{Br}_2$ for Sustainable N_2 Photofixation, *Angew. Chem. Int. Ed.* 61 (2022), <https://doi.org/10.1002/anie.202200937>.
- [31] H. Li, J. Shang, J. Shi, K. Zhao, L. Zhang, Facet-dependent Solar Ammonia Synthesis of BiOCl Nanosheets via a Proton-assisted Electron Transfer Pathway, *Nanoscale* 8 (2016) 1986–1993.
- [32] R.X. Silva, C.W.A. Paschoal, R.M. Almeida, M.C. Castro, A.P. Ayala, J.T. Auletta, M. W. Lufaso, Temperature-Dependent Raman Spectra of $\text{Bi}_2\text{Sn}_2\text{O}_7$ Ceramics, *Vib. Spectrosc.* 64 (2013) 172–177.
- [33] X. Zhang, X. Fang, X. Feng, X. Li, W. Liu, X. Xu, N. Zhang, Z. Gao, X. Wang, W. Zhou, $\text{Ni/Ln}_2\text{Zr}_2\text{O}_7$ ($\text{Ln} = \text{La}, \text{Pr}, \text{Sm}$ and Y) Catalysts for Methane Steam Reforming: the Effects of A Site Replacement, *Catal. Sci. Technol.* 7 (2017) 2729–2743.
- [34] M. Minohara, N. Kikuchi, K. Tsukuda, Y. Dobashi, A. Samizo, K. Nishio, X. He, T. Katase, T. Kamiya, Y. Aiura, Effect of Intentional Chemical Doping on Crystallographic and Electric Properties of the Pyrochlore $\text{Bi}_2\text{Sn}_2\text{O}_7$, *Mater. Des.* 216 (2022), 110549.
- [35] Y. Lu, M. Chen, T. Huang, Y. Huang, J.-j. Cao, H. Li, W. Ho, S.C. Lee, Oxygen Vacancy-dependent Photocatalytic Activity of Well-defined $\text{Bi}_2\text{Sn}_2\text{O}_7-x$ Hollow Nanocubes for NO_x Removal, *Environ. Sci.: Nano* 8 (2021) 1927–1933.
- [36] H. Yu, J. Li, Y. Zhang, S. Yang, K. Han, F. Dong, T. Ma, H. Huang, Three-in-One Oxygen Vacancies: Whole Visible-Spectrum Absorption, Efficient Charge Separation, and Surface Site Activation for Robust CO_2 Photoreduction, *Angew. Chem. Int. Ed.* 58 (2019) 3880–3884.
- [37] H. Yu, H. Huang, K. Xu, W. Hao, Y. Guo, S. Wang, X. Shen, S. Pan, Y. Zhang, Liquid-phase exfoliation into monolayered BiOBr nanosheets for photocatalytic oxidation and reduction, *ACS Sustain. Chem. Eng.* 5 (2017) 10499–10508.
- [38] G.W.K. Moore, S.E.L. Howell, M. Brady, X. Xu, K. McNeil, Anomalous collapses of nares strait ice arches leads to enhanced export of arctic sea ice, *Nat. Commun.* 12 (2021) 1.
- [39] T. Wang, C. Feng, J. Liu, D. Wang, H. Hu, J. Hu, Z. Chen, G. Xue, Bi_2WO_6 hollow microspheres with high specific surface area and oxygen vacancies for efficient photocatalysis N_2 fixation, *Chem. Eng. J.* 414 (2021), 128827.
- [40] Y. Liu, Z. Hu, J.C. Yu, Fe Enhanced Visible-Light-Driven Nitrogen Fixation on BiOBr Nanosheets, *Chem. Mater.* 32 (2020) 1488–1494.
- [41] H. Li, J. Shi, K. Zhao, L. Zhang, Sustainable Molecular Oxygen Activation with Oxygen Vacancies on the {001} Facets of BiOCl Nanosheets under Solar Light, *Nanoscale* 6 (2014) 14168–14173.
- [42] L. Huang, F. Zhang, Y. Li, P. Ding, P. Li, H. Xu, H. Li, Partial Oxidation of Sn^{2+} Induced Oxygen Vacancy Overspread on the Surface of $\text{SnO}_{2-x}/\text{g-C}_3\text{N}_4$ Composites for Enhanced LED-Light-Driven Photoactivity, *J. Inorg. Organomet. Polym. Mater.* 29 (2019) 765–775.
- [43] C. Wang, Y. Li, L. Huang, L. Yang, H. Wang, J. Liu, J. Liu, Z. Song, L. Huang, Enhanced Photocatalytic Antibacterial and Degradation Performance by n-p Type $\text{OD}/2\text{D}$ $\text{SnO}_{2-x}/\text{BiOI}$ Photocatalyst Under LED Light, *Chem. Eng. J.* 411 (2021), 128505.
- [44] Y.-J. Yuan, N. Lu, L. Bao, R. Tang, F.-G. Zhang, J. Guan, H.-D. Wang, Q.-Y. Liu, Q. Cheng, Z.-T. Yu, Z. Zou, SiP nanosheets: a metal-free two-dimensional photocatalyst for visible-light photocatalytic H_2 production and nitrogen fixation, *ACS Nano* 16 (2022) 12174–12184.
- [45] B. Huang, Y. Liu, Q. Pang, X. Zhang, H. Wang, P.K. Shen, Boosting the photocatalytic activity of mesoporous SrTiO_3 for nitrogen fixation through multiple defects and strain engineering, *J. Mater. Chem. A* 8 (2020) 22251–22256.
- [46] G. Dong, X. Huang, Y. Bi, Anchoring Black Phosphorus Quantum Dots on Fe-Doped $\text{W}_{18}\text{O}_{49}$ Nanowires for Efficient Photocatalytic Nitrogen Fixation, *Angew. Chem. Int. Ed.* 61 (2022), <https://doi.org/10.1002/anie.202204271>.
- [47] H. Bai, S.H. Lam, J. Yang, X. Cheng, S. Li, R. Jiang, L. Shao, J. Wang, A. Schottky-Barrier-Free Plasmonic Semiconductor photocatalyst for nitrogen fixation in a “one-stone-two-birds” manner, *Adv. Mater.* 34 (2022) 2104226.
- [48] H. Li, C. Mao, H. Shang, Z. Yang, Z. Ai, L. Zhang, New Opportunities for Efficient N_2 Fixation by Nanosheet Photocatalysts, *Nanoscale* 10 (2018) 15429–15435.
- [49] S. Wang, X. Hai, X. Ding, K. Chang, Y. Xiang, X. Meng, Z. Yang, H. Chen, J. Ye, Light-Switchable Oxygen Vacancies in Ultrafine $\text{Bi}_5\text{O}_7\text{Br}$ Nanotubes for Boosting Solar-Driven Nitrogen Fixation in Pure Water, *Adv. Mater.* 29 (2017) 1701774.
- [50] H. Li, J. Shang, Z. Ai, L. Zhang, Correction to “Efficient Visible Light Nitrogen Fixation with BiOBr Nanosheets of Oxygen Vacancies on the Exposed {001} Facets”, *J. Am. Chem. Soc.* 140 (2018), 526–526.
- [51] G. Li, F. Li, J. Liu, C. Fan, Fe-based MOFs for Photocatalytic N_2 Reduction: Key Role of Transition Metal Iron in Nitrogen Activation, *J. Solid State Chem.* 285 (2020), 121245.
- [52] K. Ding, A.W. Pierpont, W.W. Brennessel, G. Lukat-Rodgers, K.R. Rodgers, T. R. Cundari, E. Bill, P.L. Holland, Cobalt–dinitrogen complexes with weakened N–N bonds, *J. Am. Chem. Soc.* 131 (2009) 9471–9472.
- [53] Y. Gu, B. Xi, W. Tian, H. Zhang, Q. Fu, S. Xiong, Boosting selective nitrogen reduction via geometric coordination engineering on single-tungsten-atom catalysts, *Adv. Mater.* 33 (2021) 2100429.
- [54] M. Kunitski, N. Eicke, P. Huber, J. Köhler, S. Zeller, J. Voigtsberger, N. Schlott, K. Richs, H. Sann, F. Trinter, L.P.H. Schmidt, A. Kalinin, M.S. Schöffler, T. Jahnke, M. Lein, R. Dörner, Double-slit photoelectron interference in strong-field ionization of the neon dimer, *Nat. Commun.* 10 (2019) 1.